Axial compressive behaviour of CFDST stub columns with large void ratio

You-Fu Yang[a,*], Feng Fu[b], Xue-Meng Bie[a], Xiang-He Dai[c]

[a] *State Key Laboratory of Coastal and Offshore Engineering, Dalian University of Technology, Dalian, 116024, China*

[b] *Department of Civil Engineering, School of Mathematics, Computer Science & Engineering, City University of London, Northampton Square, London, UK*

c School of Engineering, University of Bradford, Bradford, West Yorkshire, BD7 1DP, UK

Abstract: This paper describes the experimental and numerical study on the axial compressive behaviour of circular-in-circular concrete-filled double-skin steel tube (CFDST) stub columns with large void ratio. Nine specimens with various void ratio (R_v), diameter-to-thickness ratio of outer tube (D_o/t_o) and compressive strength of concrete (f_{cu}) were tested under axial compression. The failure patterns, load versus displacement (strain) relationship, ultimate capacity and elastic composite stiffness of the specimens were investigated. The experimental results show that all specimens have good structural performance. The typical failure patterns of this new type of columns include local buckling of outer or inner tubes and crushing of concrete infill at the primary buckling locations of both tubes. It is observed from the tests that, there are three key stages in the load versus displacement (strain) relationship, namely: approximative elastic, elastoplastic and nonlinear post-peak, and with the augment of R_v and D_o/t_o and the reduce of f_{cu}, the ultimate capacity and elastic composite stiffness of the specimens decrease. Apart from tests, a finite element (FE) model was developed to further study the axial compressive behaviour of circular-in-circular CFDST stub columns with large void ratio, and the model was validated against the experimental results. Finally, a simplified analytical model to predict the ultimate capacity of circular-in-circular CFDST stub columns with large void ratio was developed, and the accuracy of the model was verified by the available experimental results. It can be used by the practising engineers in the future design of this type of columns.

Keywords: circular-in-circular CFDST stub columns; large void ratio; axial compressive behaviour; experiments; finite element (FE) model; ultimate capacity prediction.

*Corresponding author. Tel.: 86-411-8470 8510; Fax: 86-411-8467 4141.
E–mail address: youfuyang@163.com (Dr. You-Fu Yang).

1. Introduction

Concrete-filled double-skin steel tube (CFDST), which is composed of two concentric steel tubes with different outer perimeter and concrete infill between the two tubes, is a new type of composite structure [1]. Generally, while the ultimate capacity kept constant, CFDST has wider cross-section and greater flexural stiffness than the conventional concrete-filled steel tube (CFST), as the inner steel tube replaces part of the concrete core for this new type of sections. Moreover, CFDST generally uses less materials, and therefore has lower self-weight, better fire resistance and superior seismic performance compared to the conventional CFST [2-4], especially when a higher flexural stiffness is required, such as viaduct piers, mega columns in various bridges, space structures and high-rise buildings, and so on [5, 6]. Furthermore, the CFDSTs consist of inner and/or outer stainless steel tubes with a larger internal space can be used as offshore platform legs, submarine pipelines, underground integrated pipeline corridors and cabins, etc. [7], as they can provide higher axial capacity and stiffness as well as better durability compared to the traditional steel or reinforced concrete. Nowadays, circular-in-circular CFDSTs have been employed in part of electricity poles and high-rise bridge piers [8, 9], in which the void ratio of the CFDST members (R_{v}) is determined in accordance to design guidelines [4], and R_{v} is defined as $D_{\mathrm{i}}/(D_{\mathrm{o}} - 2t_{\mathrm{o}})$, where D_{i} and D_{o} are the outer diameter of inner and outer tube respectively, and t_{o} is the thickness of outer tube.

In order to well assist the engineering practice, researchers have conducted comprehensive studies on the structural behaviour of CFDST members, joints and frames while subjected to different loading cases, such as short-term static loading [5, 6, 10-12], long-term sustained loads [13], axial and lateral partial compression [14, 15], dynamic loading [16-18], fire exposure [2, 19, 20], etc. Moreover, specification or guidelines [4, 21] for the design of CFDST structures have also been issued.

However, previous studies and available design specification or guidelines focus more on the CFDST members with a relatively small R_{v} (i.e. $R_{\mathrm{v}} \leq 0.75$). A review of the literature indicates that, there are only a few experimental researches related to circular-in-circular CFDST stub columns with R_{v} larger than or equal to 0.8, including 10 specimens using polymer concrete with R_{v} of 0.8

to 0.88 [22], 2 specimens using normal concrete with R_{v} of 0.8 [23], 2 specimens using grout with R_{v} of 0.87 [24], and 4 specimens using grout with R_{v} of 0.84 to 0.92 [25], and the variation of R_{v} with D_{o} of the existing specimens is displayed in Fig. 1(a). It is shown that, D_{o} of the specimens with $R_{\mathrm{v}} \geq 0.8$ is generally smaller than 200 mm, and only Li et al. [25] reported two specimens with D_{o} of 450 mm and R_{v} of 0.92; however, the infill between two tubes was the grout. In addition, the variation of capacity index (CI) with D_{o} is demonstrated in Fig. 1(b), and CI is defined as $N_{\mathrm{ue}}/(f_{\mathrm{yo}} \cdot A_{\mathrm{so}} + f_{\mathrm{yi}} \cdot A_{\mathrm{si}} + f_{\mathrm{c}}' \cdot A_{\mathrm{c}})$, where N_{ue} is the experimental ultimate capacity, f_{yo} and f_{yi} are the yield strength of outer and inner tube respectively, A_{so} and A_{si} are the area of outer and inner tube respectively, f_{c}' is the cylindrical compressive strength of concrete, and A_{c} is the area of concrete. The results in Fig. 1(b) demonstrate that, CI has no consistent variation tendency with the increase of D_{o}, which means that there is no obvious size effect within D_{o} range of the existing specimens. Most recently, Wang et al. [7] carried out the finite element (FE) modelling of the CFDST stub columns consisting of outer stainless and inner carbon steel tubes, and the maximum void ratio and outside diameter of the models reached to 0.9 and 220 mm, respectively.

Therefore, further studies are needed to evaluate the structural performance of CFDST members with large void ratio beyond the current limit stipulated in the design specification or guidelines and to propose a new limit on the void ratio. An investigation into axial compressive behaviour of circular-in-circular CFDST stub columns with large void ratio is presented in this paper. The influence of void ratio (R_{v}), diameter-to-thickness ratio of outer tube ($D_{\mathrm{o}}/t_{\mathrm{o}}$) and compressive strength of concrete (f_{cu}) on the static performance of axially compressed CFDST stub column specimens was experimentally studied. A nonlinear FE model was also constructed using ABAQUS [26] to simulate the responses of circular-in-circular CFDST stub columns with large void ratio while subjected to axial compression, with its accuracy verified by the experimental results. Eventually, a simplified analytical model for predicting the ultimate capacity of circular-in-circular CFDST stub columns with large void ratio was developed.

2. Experimental investigation

2.1 Specimens

Nine circular-in-circular CFDST stub column specimens, consisting of outer and inner steel tubes of circular hollow section (CHS) and concrete infill between them, were tested. Fig. 2 illustrates the cross-section of the specimens, where t_{i} is the thickness of inner steel CHS. All specimens had the identical height (H) of 1500 mm. The outside diameter of the specimens was 538 mm to achieve a large void ratio, which represents the actual section size of the CFDST members in some practical construction projects. The design parameters of the specimens are presented in Table 1, where f_{cu} is the cubic compressive strength of concrete while conducting the axial compressive tests of the CFDST stub columns, K_{e} is the elastic compressive stiffness of the specimens, and N_{ufe} is the simulated ultimate capacity based on the FE method described below.

The experiment was performed to investigate the influence of R_{v} (from 0.8 to 0.9), $D_{\mathrm{o}}/t_{\mathrm{o}}$ (95.6 and 143.1) and f_{cu} (66.6 MPa and 49.4 MPa) on the behaviour of axially compressed circular-in-circular CFDST stub columns with large void ratio.

Outer and inner CHSs were all manufactured by rolling a mild steel sheet of fixed sizes and welding with one straight butt weld, and the circumferential difference between the weld of the inner and outer steel CHSs was about 90 degrees (see Fig. 2). The welding was conducted by using the electrodes having nominal yield stress, ultimate stress and elongation of 330 MPa, 415 MPa and 22%, respectively. The quality of welding was controlled carefully to ensure effective force transmission. To facilitate the casting of concrete, one circular endplate with diameter slightly larger than D_{o} and thickness of 15 mm was welded to one end of the outer and inner steel CHSs simultaneously. After curing the concrete for 14 days, the top surface of the concrete infill was polished to level with both steel CHSs to ensure that both steel CHSs and the concrete infill could bear the external loads together. In addition, to prevent damage at the loading end, therefore to control the loading process effectively, two circular steel sleeves with adjustable diameters and height of 100 mm were used for restraining the local deformation of the specimen ends.

2.2 Material properties

Carbon steel sheets of different thickness were used for fabricating the CHSs. The properties of steel were acquired by the standard tension coupon tests performed on three specimens, and the measured average values of thickness, yield strength (f_{y}), tensile strength (f_{u}), modulus of elasticity (E_{s}), Poisson's ratio (μ_{s}) and elongation after fracture (δ_{ef}) are presented in Table 2.

Two concrete mixes were produced to fill into the gap between the inner and outer steel CHSs, and the mix proportions of concrete are given in Table 3. Portland cement of 42.5 grade, limestone gravel having particle size of 5-10 mm, river sand, running water and high range water-reducing admixture (Standard Type) were used in producing the concrete. The properties of concrete are presented in Table 3, where $f_{\mathrm{cu,28}}$ and f_{cu} are the cubic compressive strength at 28-day and while the tests of CFDST stub column specimens conducted.

2.3 Test set-up and instrumentation

Fig. 3 demonstrates the test set-up for circular-in-circular CFDST stub column specimens under axial compression, and the tests were carried out by a 10,000 kN capacity tester. To monitor the strains and axial displacements, on the outside surface of the outer steel CHS, two cross-sections (S1 and S2) with 4 measuring points along the circumference with 90 degrees apart were chosen to paste the axial and hoop strain gauges (SGs), and there were four displacement transducers (DT) on the lower platen of the tester, as shown in Fig. 3. One load cell was used to gather the varied compressive loads. It should be noted that, a rigid plate consisting of four 20 mm thick steel plates welded together was placed between the upper platen of the tester and the top endplate of the steel sleeve to ensure uniform loading upon the cross-section, considering that the outside diameter of the load cell is smaller than the inner diameter of the inner steel CHS of the specimens.

The specimens were continuously loaded until the tests were terminated, and the history of loads and deformations (axial displacements and strains) and the failure process of the specimens were recorded in time. Displacement control method was adopted in this study, i.e., the displacement rate equaled to 0.2 mm/min before reaching the peak load, whilst it was equal to 1.0 mm/min after the peak load was achieved. The tests were terminated when the axial displacement reached one fortieth of the height, or in the post-peak stage the load on the specimen was less than 60% of the measured peak load.

2.4 Test results and discussion

Generally, with the increase of the axial displacements, the loads undertaken by the specimens experienced three key stages of change, i.e., approximately linear increment in the range of 50~60% of the peak load, subsequent nonlinear increment until the peak load and nonlinear reduction after achieving the peak load, and all specimens had good load-carrying capacity and deformability. Simultaneously, when the load reached 80~90% of the peak load, the outer tube began to buckle locally in a number of positions together with the sound of concrete crushing, and in the post-peak phase the buckling range and deformation of the outer tube grew rapidly while increasing the axial displacements.

The final failure pattern of the specimens (see Fig. 4) was manifested as outward local buckling (i.e. elephant's foot buckling) of the outer steel CHS (indicated by arrows), and slant of the upper endplate as there is a spherical hinge on the upper platen of the tester. For the specimens having $D_{\mathrm{o}}/t_{\mathrm{o}} = 143.1$ (Groups Aa and Ab), R_{v} and f_{cu} generally have no obvious impact on the mode and position of local buckling of outer steel CHS, i.e. elephant's foot buckling of outer steel CHS is only observed at the region near two sleeves (see Figs. 4(a) and (b)), considering that the stress state of outer tube near the sleeve is changed owing to additional lateral restraints from the sleeve, and their $D_{\mathrm{o}}/t_{\mathrm{o}}$ value is higher than the limit for the diameter-to-thickness ratio of the circular-in-circular CFDST (i.e. $135(235/f_{\mathrm{yo}})$) specified in Han et al. [4], which leads to more local buckling trend and weaker confinement to the concrete infill, and thus the outer tube cannot continue to transfer axial loads when local buckling occurs. For the specimens with $D_{\mathrm{o}}/t_{\mathrm{o}} = 95.6$ (Group Bb), elephant's foot buckling of outer steel CHS appears not only at the region near one sleeve, but also at the region near the mid-height of specimens having R_{v}=0.85 and 0.9 (see Fig. 4(c)), and the local buckling of outer steel CHS at the region near the mid-height of specimen with R_{v} of 0.9 is the most significant, i.e. R_v has an effect on the local buckling position of outer steel CHS of certain group specimens. On the one hand, the outer steel CHS with D_o/t_o lower than the specified limit has a better local stability and a stronger confinement to the concrete infill, and local buckling at the region near one sleeve cannot stop the transmission of axial loads, which may produce new local buckling at a different position, while on the other hand, with the increase of R_v, D_i/t_i of cross-section of inner tube increases and the concrete area decreases, which leads to the weakening of the local stability of inner tube and the supporting effect of concrete on the local buckling of both tubes. In addition, while keeping other parameters the same, the specimen with a smaller D_o/t_o has a smaller outward local buckling deformation of outer steel CHS, as shown in Figs. 4(b) and (c), considering that the concrete infill is better confined by the outer tube with a smaller D_o/t_o [23]. Generally, R_v and f_{cu} have no consistent effect on the local buckling deformation of outer steel CHS.

It was found that, the inner steel CHS had inward and/or outward local buckling along the height direction within the buckling range of outer tube, which indicates that the mechanical characteristics of inner steel CHS in this range is analogous to that of a steel CHS under axial compression, as typically shown in Fig. 5(a). This can be explained that, the CFDST with large void ratio has a small amount of the concrete infill, which leads to a limited volume increase of the concrete after crushing, and the outwardly buckled outer tube further reduces the effect of bulky expansion of the crushed concrete on the loading of the inner steel CHS. As can be observed in Fig. 5(b), the concrete infill generally is crushed at the buckling position of both steel CHSs due to the loss of passive confinement, and no obvious damage happens to the rest area. These phenomena have also been observed in previous experiments on axially compressed circular-in-circular CFDST stub column specimens with large void ratio [22, 23, 25].

The recorded relationship between axial displacement (Δ) and axial load (N) of the specimens are illustrated in Fig. 6 by the solid lines. It can be observed that, all $N-\Delta$ curves develop similarly and generally possess three consecutive phases, namely: approximative elastic, elastoplastic and nonlinear descent after the peak load reached. When other parameters keep constant, the growing in

R_v and $D_\mathrm{o}/t_\mathrm{o}$ produces a reduced initial slope in the approximative elastic phase of the $N-\Delta$ curves due to the overall reduction in material area and confinement of outer tube to the concrete infill, and a longer elastoplastic phase of the $N-\Delta$ curves owing to the decrease in ability to resist local instability of inner and outer steel CHS. However, f_cu has a moderate influence on the evolvement process of the first two phases of the $N-\Delta$ curves. Moreover, with the variation of three parameters considered in the tests, there is no consistent changing rule in the nonlinear descent phase after the peak load is achieved, which is mainly due to the difference in the final failure patterns and positions of the components in the specimens (see Figs. 4 and 5). In the present research, the ultimate capacity (N_ue) is considered as the peak load recorded by the $N-\Delta$ curves, and N_ue of all specimens are given in Table 1.

Fig. 7 shows axial load (N) versus strain (ε_a and ε_h) relationship of the specimens at two selected cross-sections (S1 and S2), where ε_a and ε_h represent the mean values of axial and hoop strains respectively, and ε_yo is the calculated yield strain of the outer tube and equals to $1.2\,f_\mathrm{yo}/E_\mathrm{so}$ according to the latter material constitutive relationship in the FE model, which is simplified from the measured nominal stress-strain curve, in which E_so is the modulus of elasticity of the outer tube. It is shown that, the development process of the $N-\varepsilon_\mathrm{a}(\varepsilon_\mathrm{h})$ curve is similar to that of the $N-\Delta$ curve regardless of the location of SGs, and under the same load level ε_a is larger than ε_h due to the Poisson's effect. For the selected two cross-sections of the same specimen, the $N-\varepsilon_\mathrm{a}(\varepsilon_\mathrm{h})$ curves possess similar development tendency before reaching N_ue; however, the post-peak stage of the $N-\varepsilon_\mathrm{a}(\varepsilon_\mathrm{h})$ curves shows a certain difference due to the discrepancy in the buckling positions of the outer tube. For the same cross-section, the specimen with a larger R_v has a quicker strain development under the same load owing to its lower ultimate capacity, and other two parameters have a moderate impact on the evolvement of the $N-\varepsilon_\mathrm{a}(\varepsilon_\mathrm{h})$ curves. The axial strain corresponding to N_ue is generally larger than ε_yo, which means that the outer tube shows strength failure rather than local instability failure, although $D_\mathrm{o}/t_\mathrm{o}$ of groups Aa and Ab is slightly larger than the limit specified in the design guideline [4]. It can also be found that, with the change of experimental parameters, the post-peak phase of the $N-\varepsilon_{\mathrm{a}}(\varepsilon_{\mathrm{h}})$ curves has no consistent variation rule, as the outer tube buckling positions are not completely located at the sites with strain gauges in the case of the random distribution of material defects.

Fig. 8 indicates the variation of ultimate capacity (N_{ue}) of the specimens. It is shown that, with other conditions being the same, R_{v}, $D_{\mathrm{o}}/t_{\mathrm{o}}$ and f_{cu} all have an impact on N_{ue} of the specimens. N_{ue} of the specimens decrease with the increase of R_{v} owing to the decrease in area of the concrete infill, and simultaneously the increase of inner tube area is limited. Overall, N_{ue} of the specimens with R_{v} of 0.85 and 0.9 are 9.9~14.7% and 24.3~33.3% lower than those of the specimens with R_{v}=0.8, respectively. Under the same D_{o}, the larger the $D_{\mathrm{o}}/t_{\mathrm{o}}$ of the specimens, the lower the ultimate capacity (N_{ue}), because of the relatively bigger area decrease of outer steel CHS, the worse confinement of outer steel CHS to the concrete infill and premature buckling of outer steel CHS with a larger $D_{\mathrm{o}}/t_{\mathrm{o}}$ [23]. Under the same compressive strength of concrete (i.e. $f_{\mathrm{cu}}=49.4$ MPa), the specimens with $D_{\mathrm{o}}/t_{\mathrm{o}}=143.1$ possess 10.9~16.5% lower N_{ue} values than those with $D_{\mathrm{o}}/t_{\mathrm{o}}=95.6$. Moreover, while $D_{\mathrm{o}}/t_{\mathrm{o}}$ and R_{v} kept constant, the specimens with a lower f_{cu} show a lower ultimate capacity, and N_{ue} of the specimens with $f_{\mathrm{cu}}=49.4$ MPa are 1.2~15.0% lower than those of the specimens with $f_{\mathrm{cu}}=66.6$ MPa. The above results also indicate that, compared with $D_{\mathrm{o}}/t_{\mathrm{o}}$ and f_{cu}, R_{v} is the factor that has a greater impact on the ultimate capacity of CFDST stub columns with large void ratio.

Similar to the relevant approach in previous studies [25], the elastic compressive stiffness (K_{e}) of the specimens can be obtained by the following equation:

$$K_{\mathrm{e}}=\frac{0.4N_{\mathrm{ue}}}{|\varepsilon_{\mathrm{a,0.4}}|} \tag{1}$$

in which, $\varepsilon_{\mathrm{a,0.4}}$ is the measured axial strain corresponding to $0.4N_{\mathrm{ue}}$ in the ascending phase of the $N-\varepsilon_{\mathrm{a}}$ curve. The value of K_{e} is given in Table 1.

At the same time, the elastic compressive stiffness of circular-in-circular CFDST cross-section (K_0) used in the design [4, 21] equals to the sum of the elastic compressive stiffness of its three components, and the formula is as follows:

$$K_0 = E_{so} \cdot A_{so} + E_c \cdot A_c + E_{si} \cdot A_{si} \quad (2)$$

where, E_c and E_{si} are the modulus of elasticity of the concrete infill and inner tube, respectively.

The influence of parameters on K_e and D_K is demonstrated in Fig. 9, where D_K is the ratio of K_e to K_0. The results in Fig. 9 and Table 1 show that, K_e of the specimens generally decrease with the increase of R_v and D_o/t_o and increase with the increase of f_{cu} as the area of both tubes and concrete infill varied with the variation of three parameters. K_e of the specimens with R_v of 0.85 and 0.9 are 7.6~21.2% and 27.4~35.2% lower than those of the specimens with R_v=0.8, respectively. In general, the specimens with f_{cu} of 49.4 MPa have 3.5~17.7% lower K_e values than the relavant specimens with $f_{cu} = 66.6$ MPa, and K_e of the specimens with $D_o/t_o = 143.1$ are 12.7~20.8% lower than those of the specimens with $D_o/t_o = 95.6$. Moreover, the effect of three parameters on D_K is similar to their influence on K_e and in general D_K is slightly smaller than unity due to the existence of material defects and variability in material properties. The calculation results show that, D_K varies between 0.807 and 1.025, and the mean and standard deviation of D_K are equal to 0.936 and 0.079, respectively.

3. Finite element (FE) modelling

3.1. Description of the FE model

To study the axial compressive behaviour of circular-in-circular CFDST stub columns with large void ratio numerically, a nonlinear finite element (FE) model was built using ABAQUS [26].

The modulus of elasticity and Poisson's ratio of steel CHSs replicated those acquired from material characteristic tests. The inelastic behaviour of steel CHSs was described by the classical metal plasticity model available in ABAQUS [26]. The relationship between plastic strain and true stress of steel that needs to be imported into the software was obtained based on the nominal one including five phases [7], and the detailed formulae are as follows:

$$\sigma_s = \begin{cases} E_s \cdot \varepsilon_s & (\varepsilon_s \leq \varepsilon_e) \\ -A \cdot \varepsilon_s^2 + B \cdot \varepsilon_s + C & (\varepsilon_e < \varepsilon_s \leq \varepsilon_y) \\ f_y & (\varepsilon_y < \varepsilon_s \leq \varepsilon_q) \\ f_y \cdot \left(1 + 0.6 \frac{\varepsilon_s - \varepsilon_q}{\varepsilon_u - \varepsilon_q}\right) & (\varepsilon_q < \varepsilon_s \leq \varepsilon_u) \\ 1.6 f_y & (\varepsilon_s > \varepsilon_u) \end{cases} \tag{3}$$

where, σ_s and ε_s are the nominal stress and strain of steel respectively, $\varepsilon_e = 0.8 f_y / E_s$, $\varepsilon_y = 1.5\varepsilon_e$, $\varepsilon_q = 10\varepsilon_y$, $\varepsilon_u = 100\varepsilon_y$, $A = 0.2 f_y / (\varepsilon_y - \varepsilon_e)^2$, $B = 2A \cdot \varepsilon_y$, and $C = 0.8 f_y + A \cdot \varepsilon_e^2 - B \cdot \varepsilon_e$.

The size effect of concrete was not considered in the present FE simulation according to the analysis on the experimental data in Fig. 1(b). The modulus of elasticity and Poisson's ratio of the concrete infill were taken as $4730\sqrt{f_c'}$ [27] and 0.2 [28], respectively. The damaged plasticity model in the ABAQUS [26], including isotropic compressive/tensile plasticity as well as isotropic damaged elasticity, was chosen for describing the inelastic property of the concrete infill, in which, the equivalent compressive/tensile plastic strain were adopted to control the yield and failure surface, and the characterization of softening and stiffness deterioration was actualized by the compressive/tensile damage variables, respectively. The tension stiffening of concrete was simulated by the fracture energy cracking criterion [8]. The engineering compressive stress (σ_c) versus strain (ε_c) relationship presented by Wang et al. [7] was adopted to calculate the tabulated data for the compressive stress and the relevant inelastic strain of the concrete infill in a circular-in-circular CFDST, as presented in the following equations:

$$\sigma_c / f_c' = \begin{cases} 2\left(\varepsilon_c / \varepsilon_{c,p}\right) - \left(\varepsilon_c / \varepsilon_{c,p}\right)^2 & (\varepsilon_c / \varepsilon_{c,p} \leq 1) \\ \frac{\varepsilon_c / \varepsilon_{c,p}}{\rho \cdot \left(\varepsilon_c / \varepsilon_{c,p} - 1\right)^2 + \varepsilon_c / \varepsilon_{c,p}} & (\varepsilon_c / \varepsilon_{c,p} > 1) \end{cases} \tag{4}$$

where, $\varepsilon_{c,p} = (1300 + 12.5 f_c' + 800\xi^{0.2})/1E6$, $\rho = 0.5\sqrt{f_c'} \cdot (2.36E-5)^{[0.25+(\xi-0.5)^7]} \geq 0.12$, and ξ is the nominal confinement factor [4]. It should be noted that, the adopted engineering compressive $\sigma_c - \varepsilon_c$ relationship took into account the influence of the confinement of outer steel CHS to the concrete infill on the peak strain ($\varepsilon_{c,p}$) and the post-peak stage through variable ξ.

Outer and inner steel CHSs were simulated by S4 elements, which uses the Simpson's rule with 9 integration points in thickness direction, whilst the concrete infill and the steel sleeves (including the stiffeners and endplate on them) were modeled by C3D8R elements. In this study, the structured meshing technology available in ABAQUS was selected while the meshing size about $D_o/12$, and both steel CHSs and the concrete infill had the same mesh nodes, so as to guarantee the deformation coordination of different components of the composite columns and to improve the convergence of the FE modelling. The meshing used in the FE model is shown in Fig. 10.

The surface to surface contacts were considered in simulating the interface features between different components of the FE model. To model the interface between steel CHSs and the concrete infill, the 'hard contact' was used in the normal direction, which enables the compressive stress perpendicular to the contact surfaces to be transferred completely between the interfaces, and the contact surfaces between different components can be separated but not penetrated. At the same time, the 'Coulomb friction' model was used in the tangential directions and the friction coefficient was equal to 0.6 according to previous simulations [7, 8], i.e. the interfaces can transfer shear stresses, and relative sliding between the interfaces occurs after the shear stress reaches a critical value [26]. For the interface between the endplate on the sleeves and the concrete infill, only the 'hard contact' constraint in the normal direction was defined. Moreover, the 'shell-to-solid coupling' constraint was considered for the interface between the endplate on the sleeves and both steel CHSs, and the interface between the sleeves and outer steel CHS was defined as the 'Tie' constraint.

The FE model of the CFDST stub columns together with the sleeves was constructed using the ABAQUS Standard [26], and the boundary conditions are indicated in Fig. 10. Two reference points respectively coupled with the upper and lower endplate on the steel sleeve were set at the center of the endplates to define the boundary conditions. The 'ENCASTRE' was set to the reference point of the lower endplate, i.e. all degrees of freedom were constrained, and the reference point of the upper endplate has no translational displacement in X and Y directions, i.e. $U_X=U_Y=0$. During the loading step, axial displacements along Z direction were applied to the reference point of the upper endplate.

As is well known, the influence of initial imperfections and residual stresses on the performance of steel tubes is evident. However, the investigations of Wang et al. [7] showed that, compared with the steel CHSs, the effects of initial imperfections and residual stresses on circular CFDST stub columns were reduced by the concrete infill significantly, and thus the initial imperfections and residual stresses were not incorporated into the current FE modelling.

3.2. Verification of the FE model

Typical failure patterns of the specimens predicted by the FE model are demonstrated in Fig. 11. From the comparison between Fig. 11 and Figs. 4 and 5, it can be observed that, the FE results generally reflect the failure characteristics of the whole composite column and its components, i.e. local buckling of outer and inner tube along the circumference appear at 1~2 regions, while the concrete infill deforms obviously at the local buckling regions of both tubes irrespective of R_{v} value. However, the predicted local buckling and deformed regions are different from the experimental observations, and there is no evident rotation for the top and bottom surface of the components. This is attributed to the randomness of material defect distribution in the specimens and the inclining of top endplate to the severely damaged region of the specimens, and these cannot be considered in the current FE model.

The simulated $N-\Delta$ curves are compared with the recorded ones in Fig. 6. It is shown that, analogous to the curve of the specimens, the simulated $N-\Delta$ curve also consists of approximative elastic, elastoplastic and nonlinear post-peak stages. However, the simulated $N-\Delta$ curves possess a higher initial slope, and a slower bearing capacity descending and a more stable residual bearing capacity after achieving the peak load. It should be noted that, there are several facts in the specimens that cannot be reflected in the FE model, mainly including randomly distributed material defects, variation of material properties, clearance between steel CHSs and the concrete infill, possible non-axial compression after the peak load, etc. These cause the abovementioned disparity between two kinds of $N-\Delta$ curves. The predicted $N-\varepsilon_{\mathrm{a}}(\varepsilon_{\mathrm{h}})$ relationship at cross-section S1 are in comparison with the measured results in Fig. 12, where the letters 'M' and 'P' in the parentheses respectively denote the measured and predicted results. It is shown that, the predicted elastic stage of $N-\varepsilon_{\mathrm{a}}(\varepsilon_{\mathrm{h}})$ curves is generally in good agreement with the measured one; however, the elastoplastic and post-peak stage of the predicted curves show a certain difference with the corresponding stages of the measured results, considering that there is discrepancy between the predicted bucking positions of both tubes and the measured results, as shown in Figs. 4, 5 and 11.

The deviation between the predicted ultimate capacities by the FE model (N_{ufe}) and the measured results (N_{ue}) in this and the previous experiments is indicated in Fig. 13. In the FE simulation, polymer concrete and grout adopted in the previous tests [22, 24, 25] are temporarily treated as ordinary concrete, considering that there is currently no mature constitutive model for these two kinds of concrete. N_{ufe} of the specimens in this study are given in Table 1. An analysis of all 27 data in Fig. 13 demonstrates that, the mean and standard deviation of $N_{\mathrm{ufe}}/N_{\mathrm{ue}}$ respectively equal to 0.946 and 0.050, and the predicted ultimate capacities are generally limited to 10% of the measured results.

The above comparison and analysis indicate that, the FE model developed in this study is generally accurate to investigate the axial compressive behaviour of circular-in-circular CFDST stub columns with large void ratio.

4. Parametric study

The impact of factors on stress state of each component of the CFDST stub columns with large void ratio while reaching the ultimate capacity was further investigated by the validated FE model. The basic conditions of the computing examples included: $D_{\mathrm{o}} = 540$ mm, $H = 1500$ mm, $D_{\mathrm{i}}/t_{\mathrm{i}} = 60$, $f_{\mathrm{yo}} = f_{\mathrm{yi}} = 355$ MPa, $f_{\mathrm{c}}' = 50$ MPa, $R_{\mathrm{v}} = 0.8{\sim}0.95$, and nominal steel ratio $\alpha_{\mathrm{n}} = 0.08$, in which α_{n} equals to the ratio of A_{so} to the cross-sectional area enclosed by the inner wall of the outer steel CHS (A_{ce}) [4]. In addition, the corresponding circular CFST with the same material and geometric properties of the outer steel CHS as the circular-in-circular CFDST was also taken into account. The Mises stress of steel CHSs and the longitudinal stress (S33) of concrete at the mid-height section were obtained and analyzed.

The comparison of the Mises stress of outer steel CHS between CFDST and CFST is indicated in Fig. 14. It is shown that, the stress distribution of outer tube in the CFDST is the same as that of steel tube in the CFST, and the Mises stress in most areas of outer tube in the CFDST and CFST reaches

f_{yo}. The distribution of the Mises stress of inner steel CHS in the CFDST is similar to that of outer steel CHS, and f_{yi} can also be reached in most areas of inner tube in the CFDST, as shown in Fig. 15. The influence of parameters on $\sigma_{si,u}/f_{yi}$ of inner steel CHS is plotted in Fig. 16, in which $\sigma_{si,u}$ is the maximum Mises stress. It can be seen that, all parameters have a moderate effect on $\sigma_{si,u}/f_{yi}$, and $\sigma_{si,u}$ is slightly higher than f_{yi}.

The variation of the longitudinal stress (S33) of concrete in the CFDST with different void ratio and the CFST is demonstrated in Fig. 17. It is shown that, the S33 of all sections are larger than f_c'; however, the S33 of CFDST columns are smaller than those of the corresponding CFST columns as the confinement effect of outer tube on the concrete is reduced by the inward deformation of the concrete infill and inner tube. Furthermore, the S33 of CFDST columns is small on the inside and large on the outside; however, the S33 of CFST columns is large on the inside (center) and small on the outside (edge). This is attributed to the fact that, under the same axial deformation, the inner tube of CFDST columns deforms inwards due to the Poisson's effect and the void characteristics, which results in a weaker supporting action of inner steel CHS on the transverse deformation of concrete compared with the confinement effect of outer tube, and thus, the transverse confinement of the concrete infill is gradually reduced from the outside to the inside. However, the closer the core concrete of CFST columns is to the center, the stronger the transverse deformation is constrained by its peripheral concrete and the outer tube.

Fig. 18 indicates the effect of parameters on S_{33}/f_c' of the concrete infill in the CFDST, where D_c is the thickness of the concrete infill. It can be discovered that, in generally, R_v, α_n, f_{yo} and f_c' have significant effect on S_{33}/f_c', and D_i/t_i has a moderate influence on S_{33}/f_c'. A bigger S_{33}/f_c' is caused with the increase of α_n and f_{yo} and decrease of f_c'. In addition, due to the difference between the supporting action of inner tube and the confinement effect of outer tube to the concrete infill, S_{33}/f_c' on the side near the inner edge increases with the increase of R_v, whilst S_{33}/f_c' on the side near the outer edge decreases with the increase of R_v.

5. Ultimate capacity prediction

Based on the results in this study (see Figs. 15 and 16) and the suggestions in the literature [4], it is assumed that, the axial stress of inner steel CHS equals to its yield strength (f_{yi}) when reaching the ultimate capacity of axially compressed circular-in-circular CFDST stub columns with large void ratio. As a result, the composite strength index ($f_{\mathrm{scy,v}}$) can be defined as follows:

$$f_{\mathrm{scy,v}}=\frac{N_{\mathrm{u}}-f_{\mathrm{yi}}\cdot A_{\mathrm{si}}}{A_{\mathrm{so}}+A_{\mathrm{c}}} \tag{5}$$

where, N_{u} is the ultimate capacity obtained by the FE simulation.

The FE modelling results show that, the parameters that have an important effect on $f_{\mathrm{scy,v}}$ include R_{v}, α_{n}, f_{yo} and f_{c}', as indicated by the solid lines in Fig. 19, and $f_{\mathrm{scy,v}}$ augments with the increase of R_{v}, α_{n} and f_{yo} and decrease of f_{c}'. By regressing the data in Fig. 19 and referring to the formulae of such composite columns with small void ratio [4], it is found that, in general, the formula that applies to circular-in-circular CFDST stub columns with $R_{\mathrm{v}}\leq 0.75$ can also be applied to those with large void ratio, and the equation is:

$$f_{\mathrm{scy,v}}=\frac{\alpha}{1+\alpha}\cdot R_{\mathrm{v}}^{2}\cdot f_{\mathrm{yo}}+\frac{1+\alpha_{\mathrm{n}}}{1+\alpha}\cdot(1.14+1.02\xi)\cdot f_{\mathrm{ck}} \tag{6}$$

in which, α ($=A_{\mathrm{so}}/A_{\mathrm{c}}$) is the steel ratio, and f_{ck} is the characteristic compressive strength of concrete [4].

Fig. 19 indicates the comparison between the simplified and numerical $f_{\mathrm{scy,v}}$. It is shown that, the simplified results accord well with the numerical ones, which indicates that Eq. (6) can predict the composite strength index of circular-in-circular CFDST stub columns with large void ratio well. Therefore, by substituting Eq. (6) into Eq. (5), the model for the ultimate capacity prediction of axially compressed circular-in-circular CFDST stub columns with large void ratio can be obtained:

$$N_{\mathrm{u}}=\left[\frac{\alpha}{1+\alpha}\cdot R_{\mathrm{v}}^{2}\cdot f_{\mathrm{yo}}+\frac{1+\alpha_{\mathrm{n}}}{1+\alpha}\cdot(1.14+1.02\xi)\cdot f_{\mathrm{ck}}\right]\cdot(A_{\mathrm{so}}+A_{\mathrm{c}})+f_{\mathrm{yi}}\cdot A_{\mathrm{si}} \tag{7}$$

The influence of R_{v} on $N_{\mathrm{us}}/N_{\mathrm{ue}}$ of circular-in-circular CFDST stub columns with large void ratio is plotted in Fig. 20, where N_{us} is the simplified ultimate capacity based on Eq. (7), and a total of 27 data from the literature and this study are covered. The results indicate that, the minimum and maximum values of $N_{\mathrm{us}}/N_{\mathrm{ue}}$ are 0.851 and 1.044, respectively, while the mean and standard deviation are 0.939 and 0.051, respectively. As a result, the simplified model is suitable for the ultimate capacity prediction of axially compressed circular-in-circular CFDST stub columns with void ratio extended to 0.95 and generally tends to be safe. The range of valid parameters applicable to Eq. (7) is: $R_{\mathrm{v}} = 0{\sim}0.95$, $\alpha_{\mathrm{n}} = 0.04{\sim}0.12$, $f_{\mathrm{yo}}(f_{\mathrm{yi}}) = 235{\sim}460$ MPa, $f_{\mathrm{c}}' = 25{\sim}75$ MPa and $D_{\mathrm{i}}/t_{\mathrm{i}} = 30{\sim}90$.

6. Conclusions

According to the experimental study and finite element (FE) simulation on axial compressive behaviour of circular-in-circular CFDST stub columns with large void ratio presented in this study, the following conclusions can be achieved:

(1) After the tests completed, the outer steel CHS mainly buckles outward at the region near the sleeve, while the outer tube of the specimens with a smaller $D_{\mathrm{o}}/t_{\mathrm{o}}$ and R_{v} of 0.8 and 0.9 also buckles outward at the mid-height region, and a smaller $D_{\mathrm{o}}/t_{\mathrm{o}}$ leads to a smaller outward buckling deformation. Simultaneously, the inner steel CHS buckles inward and/or outward along the height direction within the buckling range of the outer tube. Moreover, at the primary buckling area of both steel CHSs, crushing of the concrete infill appears.

(2) Generally, there are three key stages in the $N-\Delta(\varepsilon)$ curve of the specimens, namely: approximative elastic, elastoplastic and nonlinear post-peak. R_{v} and $D_{\mathrm{o}}/t_{\mathrm{o}}$ have obvious effect on the ascending stage of the curve, and all three parameters have no consistent effect on the nonlinear post-peak stage of the curve due to the difference in the final failure positions and patterns of the components. Moreover, a higher R_{v} results in a quicker strain development, and other two parameters have a moderate impact on the evolvement of the $N-\varepsilon$ curves.

(3) While other parameters kept constant, N_{ue} and K_{e} of circular-in-circular CFDST stub column specimens with large void ratio decrease with the augment of R_{v} and $D_{\mathrm{o}}/t_{\mathrm{o}}$ and the reduce of f_{cu}. $N_{\mathrm{ue}}(K_{\mathrm{e}})$ of the specimens with R_{v} of 0.85 and 0.9 are 9.9~14.7% (7.6~21.2%) and 24.3~33.3% (27.4~35.2%) lower than those of the specimens with R_{v}=0.8 respectively, and the specimens with a larger $D_{\mathrm{o}}/t_{\mathrm{o}}$ and a lower f_{cu} possess 10.9~16.5% (12.7~20.8%) and 1.2~15.0%

(3.5~17.7%) lower $N_{\mathrm{ue}}(K_{\mathrm{e}})$, respectively. Furthermore, the measured elastic compressive stiffness of the specimens are generally close to the calculated values according to the design method.

(4) The FE model built using the ABAQUS is generally accurate to predict the failure patterns, the load versus displacement (strain) curves and the ultimate capacity of axially compressed circular-in-circular CFDST stub column specimens with large void ratio.

(5) Based on the stress distribution characteristics of both steel CHSs and the concrete infill simulated by the FE model, the calculation model for the ultimate capacity of axially compressed circular-in-circular CFDST stub column specimens with large void ratio is developed, from which the calculated ultimate capacities accord well with the measured results.

It is apparent that the CFDST members may be subjected to unbalanced bending moments in addition to axial forces. In the future, further investigations into the performance of CFDST beams and beam-columns with large void ratio are needed to guide the design and application of such new composite sections.

Declaration of Competing Interest

The authors declare that they have no known competing financial interests or personal relationships that could have appeared to influence the work reported in this paper.

Acknowledgements

The studies in this paper are financially supported by the National Natural Science Foundation of China (Grant No. 51678105). The financial support is gratefully acknowledged. The authors also wish to thank Mr. Lin-Lin Sun for her assistance in the experiments.

References:

[1] L. H. Han, Y. F. Yang, H. Yang, W. Li, Life-cycle based analytical theory of concrete-filled steel tubular structures and its applications, Chin. Sci. Bull. 65(28-29) (2020) 3173-3184. (in Chinese)

[2] A. L. Camargo, J. P. C. Rodrigues, R. H. Fakury, L. Laim, Fire resistance of axially and rotationally restrained concrete-filled double-skin and double-tube hollow steel columns, J. Struct. Eng. 145(11) (2019) 04019128.

[3] L. H. Han, H. Huang, Z. Tao, X. L. Zhao, Concrete-filled double skin steel tubular (CFDST) beam-columns subjected to cyclic bending, Eng. Struct. 28(12) (2006) 1698-1714.

[4] L.H. Han, D. Lam, D.A. Nethercot, Design Guide for Concrete-Filled Double Skin Steel Tubular Structures, CRC Press, UK, 2018.

[5] P. Ayough, N. H .R. Sulong, Z. Ibrahim, Analysis and review of concrete-filled double skin steel tubes under compression, Thin-Walled Struct. 148 (2020) 106495.

[6] S. Vernardos, C. Gantes, Experimental behavior of concrete-filled double-skin steel tubular (CFDST) stub members under axial compression: A comparative review, Structures 22 (2019) 383-404.

[7] F. C. Wang, L. H. Han, W. Li, Analytical behavior of CFDST stub columns with external stainless steel tubes under axial compression, Thin-Walled Struct. 127 (2018) 756-768.

[8] W. Li, L. H. Han, T.M. Chan, Numerical investigation on the performance of concrete-filled double-skin steel tubular members under tension, Thin-Walled Struct. 79 (2014) 108-118.

[9] F. Yagishita, H. Kitoh, M. Sugimoto, T. Tanihira, K. Sonoda, Double skin composite tubular columns subjected to cyclic horizontal force and constant axial force, Proceedings of the 6th International Conference on Advances in Steel and Concrete Composite Structures 2000, pp. 497-503.

[10] F. X. Ding, W. J. Wang, D. R. Lu, X. M. Liu, Study on the behavior of concrete-filled square double-skin steel tubular stub columns under axial loading, Structures 23 (2020) 665-676.

[11] C. Hou, L. H. Han, T. M. Mu, Behaviour of CFDST chord to CHS brace composite K-joints: Experiments, J. Constr. Steel. Res. 135 (2017) 97-109.

[12] Y. F. Yang, C. Shi, C. Hou, Experimental and numerical study on static behaviour of uniplanar CFDST-CHS T-joints, J. Constr. Steel Res. 173 (2020) 106250.

[13] L. H. Han, Y. J. Li, F. Y. Liao, Concrete-filled double skin steel tubular (CFDST) columns subjected to long-term sustained loading, Thin-Walled Struct. 49(12) (2011) 1534-1543.

[14] C. Hou, L. H. Han, X. L. Zhao, Behaviour of circular concrete filled double skin tubes subjected to local bearing force, Thin-Walled Struct. 93 (2015) 36-53.

[15] Y. F. Yang, L. H. Han, B. H. Sun, Experimental behaviour of partially loaded concrete filled double-skin steel tube (CFDST) sections, J. Constr. Steel. Res. 71 (2012) 63-73.

[16] Y. Hu, J. Zhao, D. Zhang, H. Zhang, Cyclic tests of fully prefabricated concrete-filled double-skin steel tube/moment-resisting frames with beam-only-connected steel plate shear walls, Thin-Walled Struct. 146 (2020) 106272.

[17] W. Li, Y. Z. Gu, L. H. Han, X. L. Zhao, Behaviour of grout-filled double-skin steel tubular T-joint subjected to low-velocity impact, Thin-Walled Struct. 144 (2019) 106270.

[18] F. Zhou, W. Xu, Cyclic loading tests on concrete-filled double-skin (SHS outer and CHS inner) stainless steel tubular beam-columns, Eng. Struct. 127 (2016) 304-318.

[19] R. Imani, G. Mosqueda, M. Bruneau, Experimental study on post-earthquake fire resistance of ductile concrete-filled double-skin tube columns, J. Struct. Eng. 141(8) (2015): 04014192.

[20] M. L. Romero, C. Ibañez, A. Espinos, J. M. Portolés, A. Hospitaler, Influence of ultrahigh strength concrete on circular concrete-filled dual steel columns, Structures 9 (2017) 13-20.

[21] China Civil Engineering Society (CCES), Technical Specification for Concrete-filled Double Skin Steel Tubular Structures (T/CCES 7-2020), China Architecture & Building Press, Beijing, 2020 (in Chinese).

[22] S. Wei, S. T. Mau, C. Vipulanandan, S. K. Mantrala, Performance of new sandwich tube under axial loading: experiment, J. Struct. Eng. 121(12) (1995) 1806-1814.

[23] Z. Tao, L. H. Han, X. L. Zhao, Behaviour of concrete-filled double skin (CHS inner and CHS outer) steel tubular stub columns and beam-columns, J. Constr. Steel Res. 60(8) (2004) 1129-1158.

[24] C. Keindorf, P. Schaumann, Sandwichtowers for wind turbines with high strength steel and core materials, Stahlbau 79(9) (2010) 648-659.

[25] W. Li, D. Wang, L. H. Han, Behaviour of grout-filled double skin steel tubes under compression and bending: Experiments, Thin-Walled Struct. 116 (2017) 307-319.

[26] Simulia, ABAQUS Analysis User's Guide, Version 6.14, Dassault Systèmes Simulia Corp, Providence, RI, 2014.

[27] ACI Committee 318, Building Code Requirements for Structural Concrete (ACI 318-19) and Commentary, American Concrete Institute, Detroit, USA, 2019.

[28] FIB, Fib Model Code for Concrete Structures 2010, Fédération Internationale du Béton, Ernst & Sohn, Berlin, Germany, 2013.

Figures:

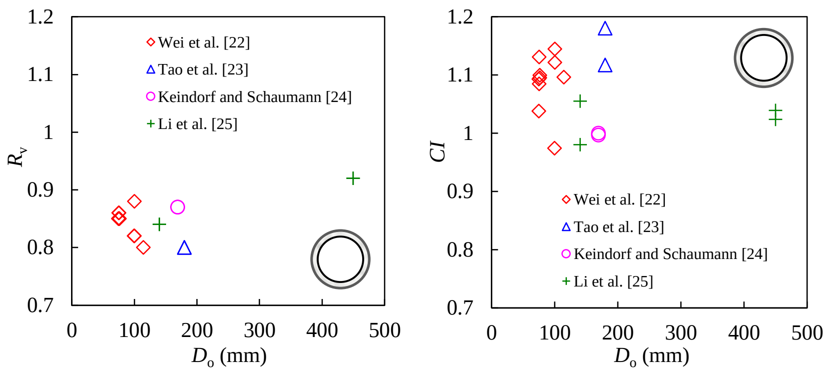

(a) Variation of R_v with D_o (b) Variation of CI with D_o

Fig. 1. Test data in the literature.

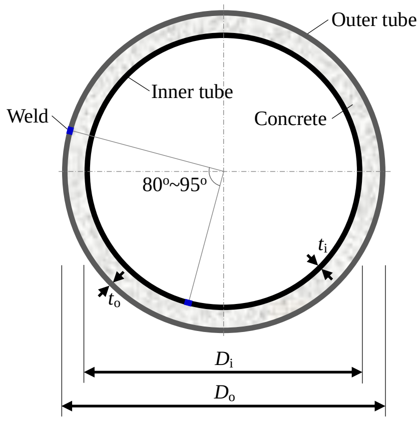

Fig. 2. Cross-section of the specimens.

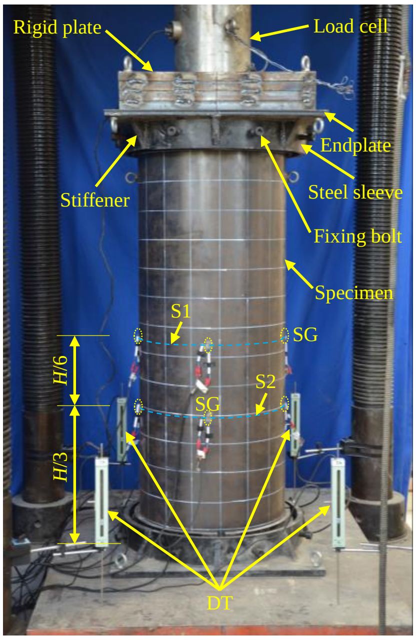

Fig. 3. Picture of test set-up and instrumentations.

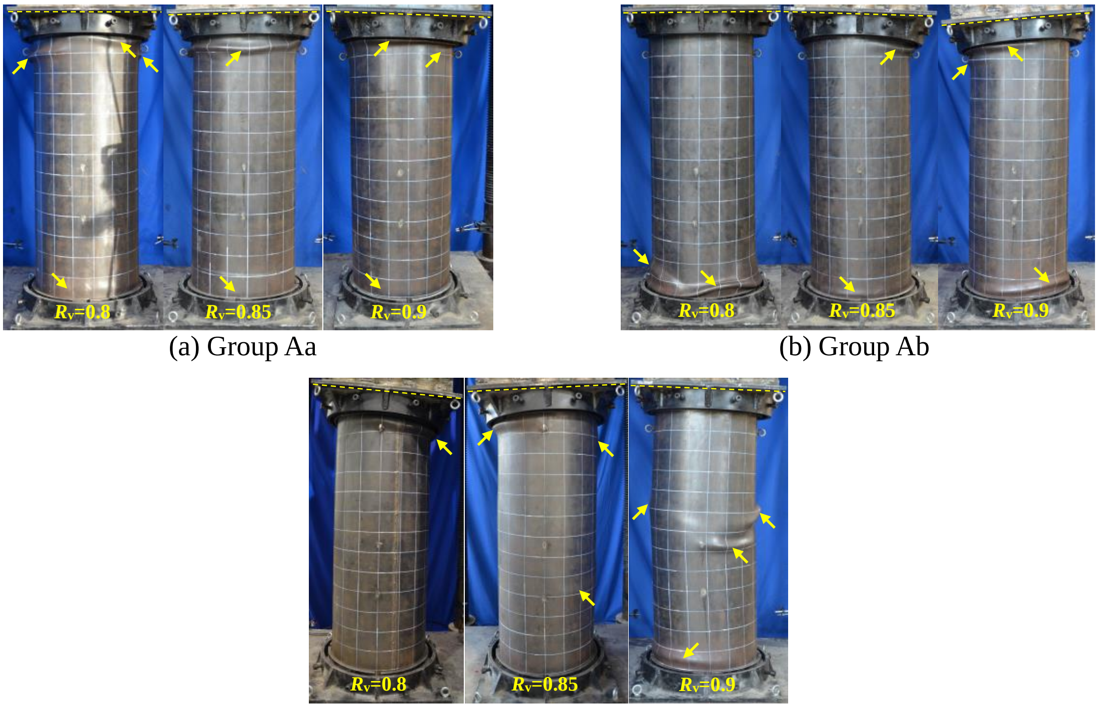

(a) Group Aa

(b) Group Ab

(c) Group Bb

Fig. 4. Failure pattern of the specimens.

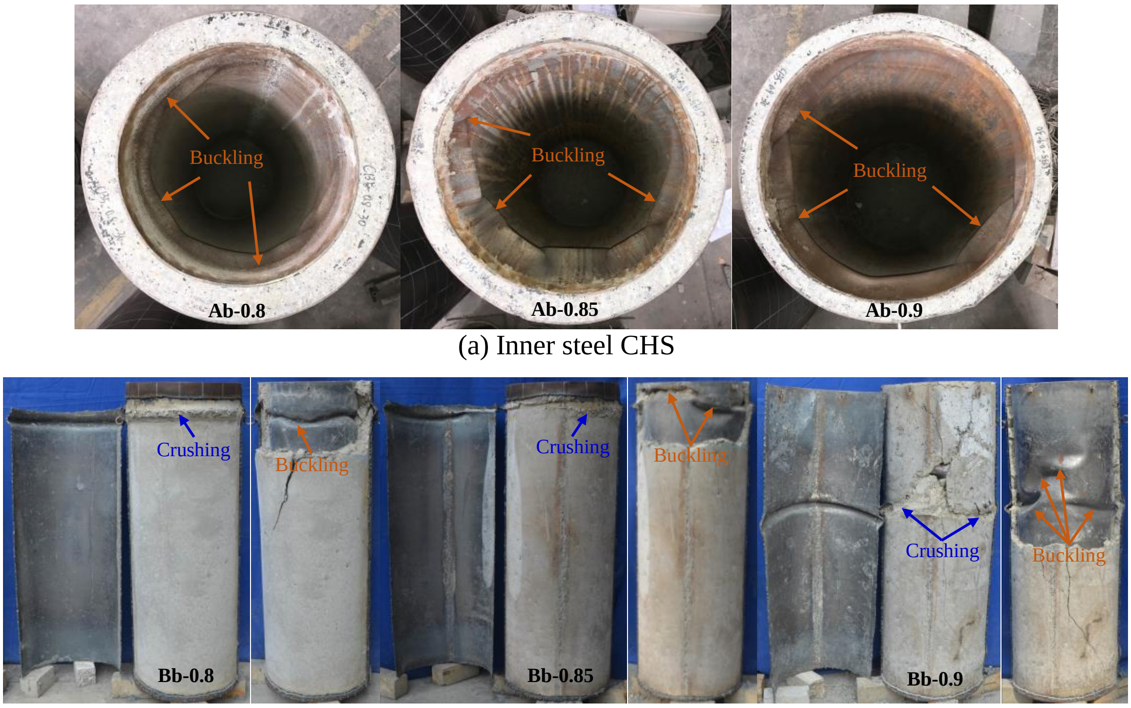

(a) Inner steel CHS

(b) The concrete infill

Fig. 5. Typical failure pattern of two internal components.

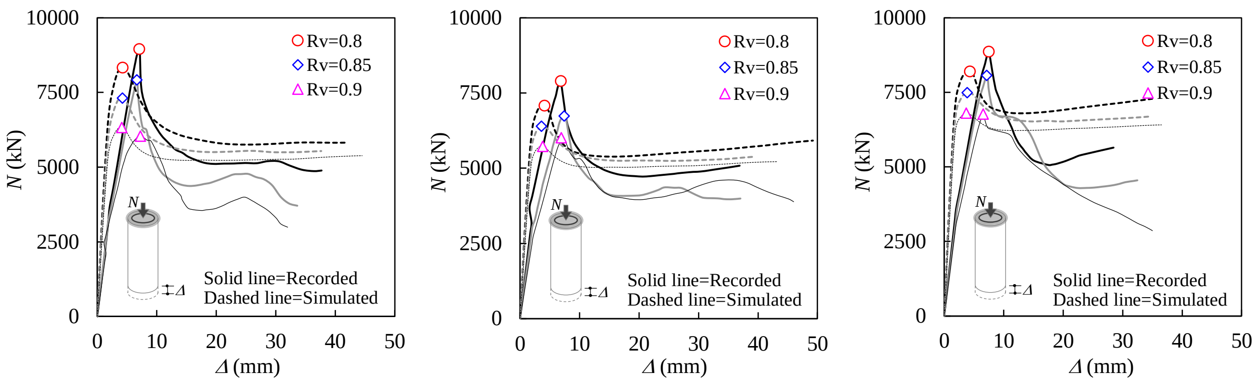

(a) Group Aa (b) Group Ab (c) Group Bb

Fig. 6. $N - \Delta$ relationship of the specimens.

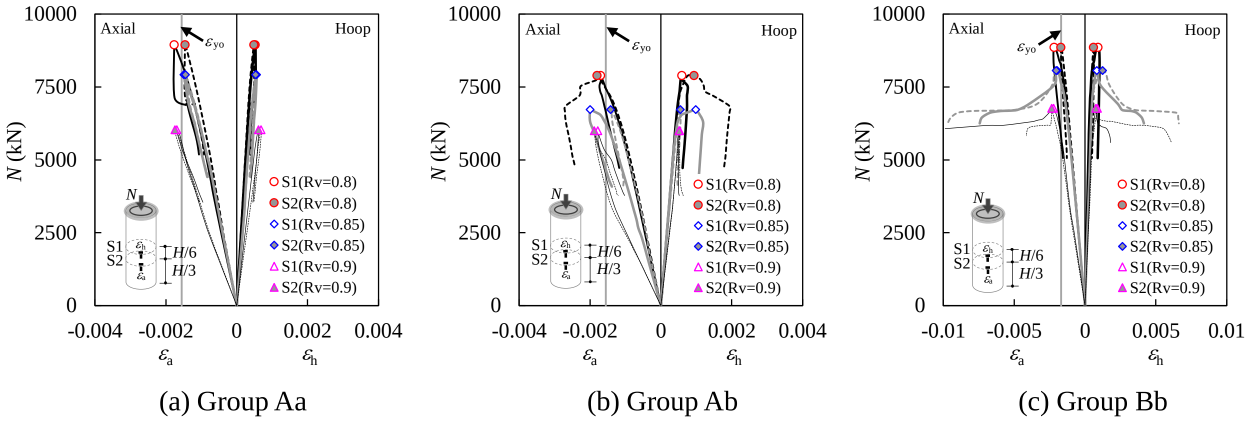

Fig. 7. Axial load (N) versus strain (ε_{a} and ε_{h}) relationship of the specimens.

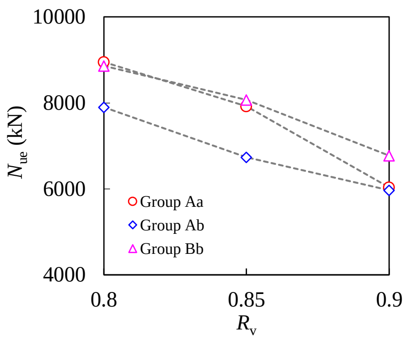

Fig. 8. Variation of N_{ue}.

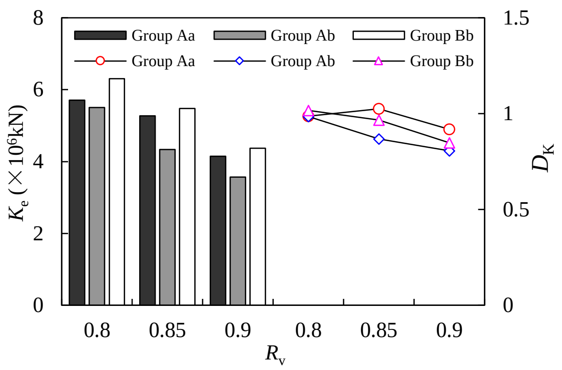

Fig. 9. Influence of parameters on K_{e} and D_{k}.

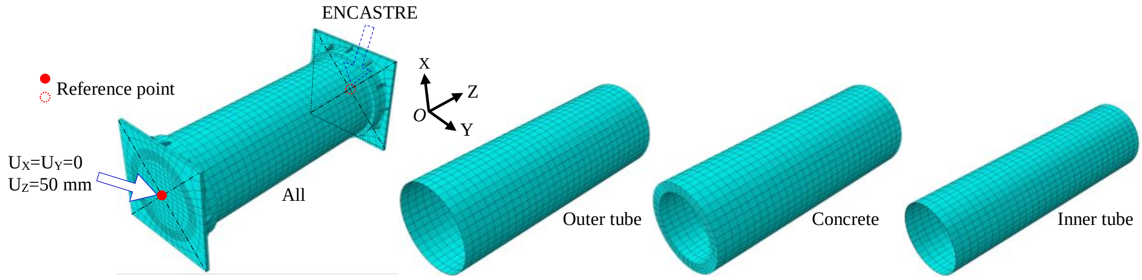

Fig. 10. Meshing and boundary conditions of the FE model.

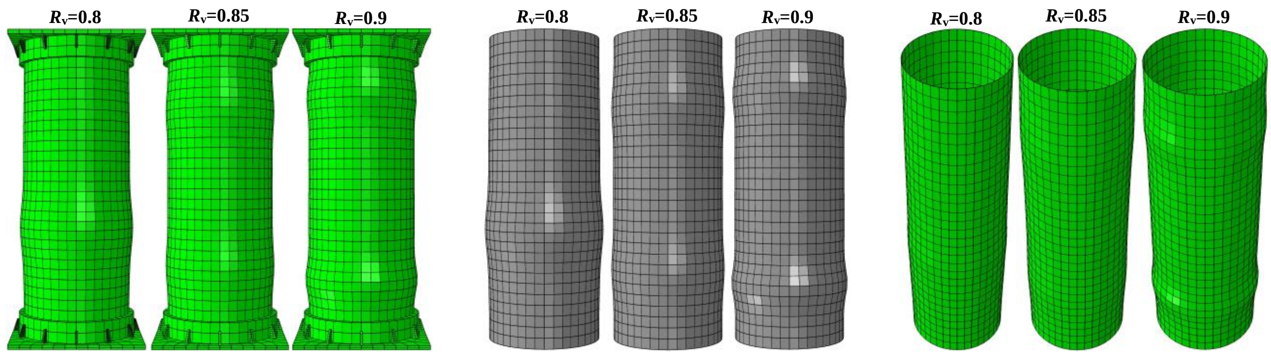

(a) Overall (b) The concrete infill (c) Inner steel CHS

Fig. 11. Typical failure patterns of the specimens predicted by the FE model.

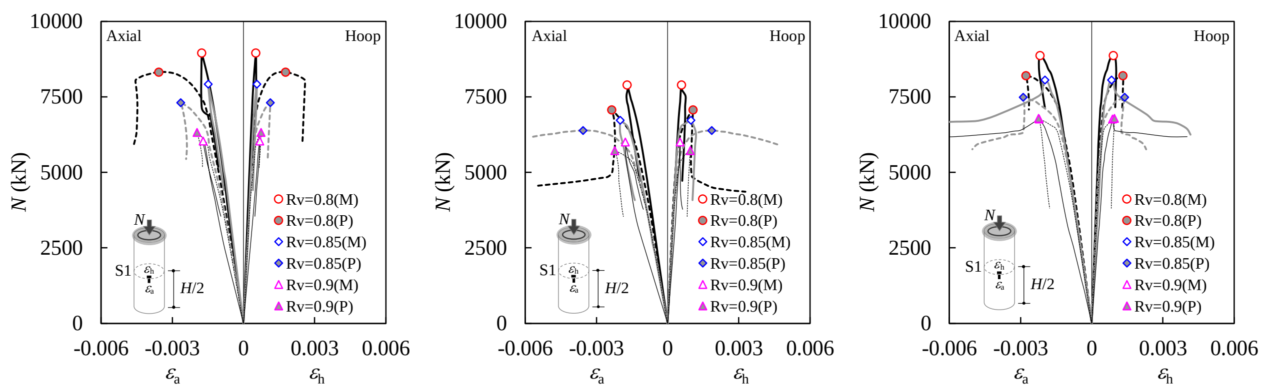

(a) Group Aa (b) Group Ab (c) Group Bb

Fig. 12. Comparison between the predicted and measured $N-\varepsilon_a(\varepsilon_h)$ relationship at section S1.

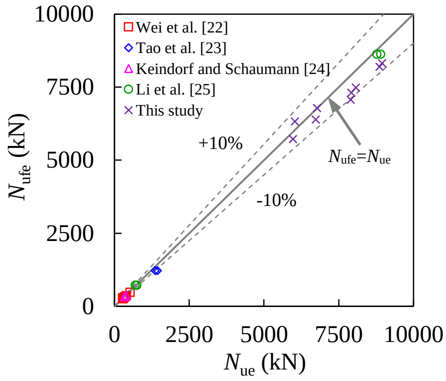

Fig. 13. Deviation between the predicted and measured ultimate capacities.

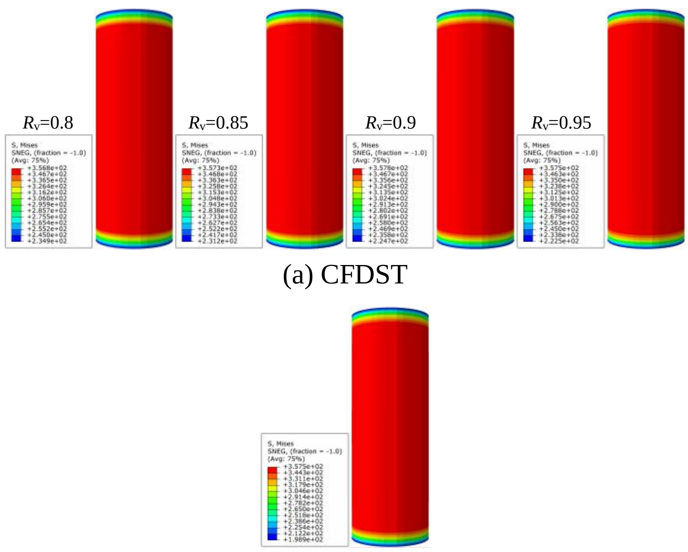

(a) CFDST

(b) CFST

Fig. 14. Comparison of the Mises stress of outer tube between CFDST and CFST.

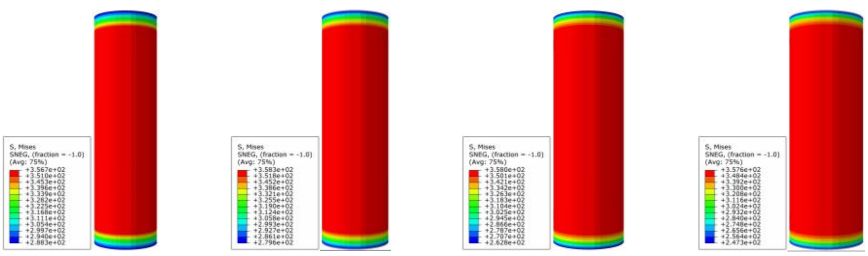

(a) R_v=0.8 (b) R_v=0.85 (c) R_v=0.9 (d) R_v=0.95

Fig. 15. The Mises stress of inner tube of CFDST.

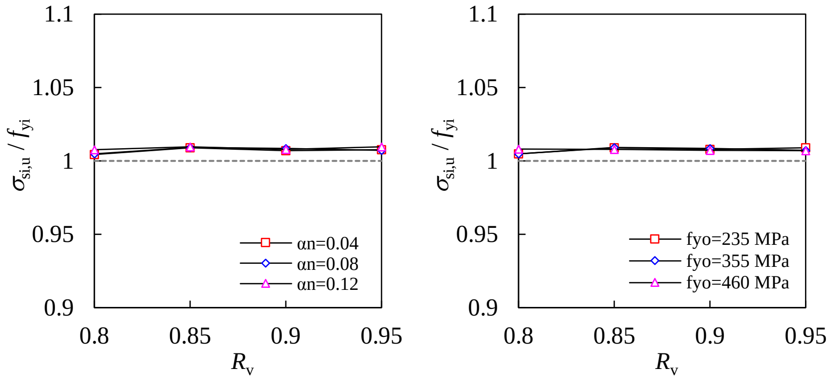

(a) α_n (b) f_{yo}

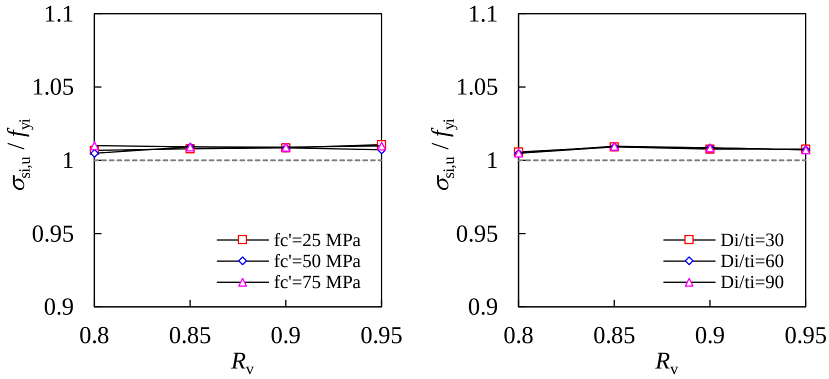

(c) f_c' (d) D_i/t_i

Fig. 16. Influence of parameters on $\sigma_{si,u}/f_{yi}$ of inner steel CHS.

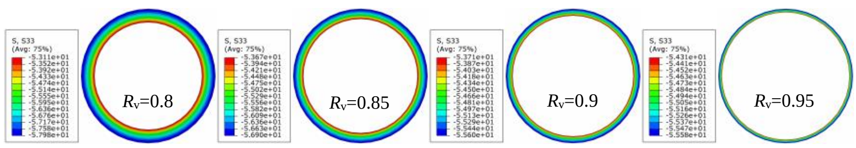

(a) CFDST

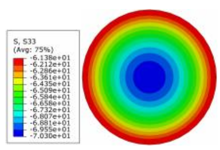

(b) CFST

Fig. 17. Variation of the longitudinal stress (S33) of concrete.

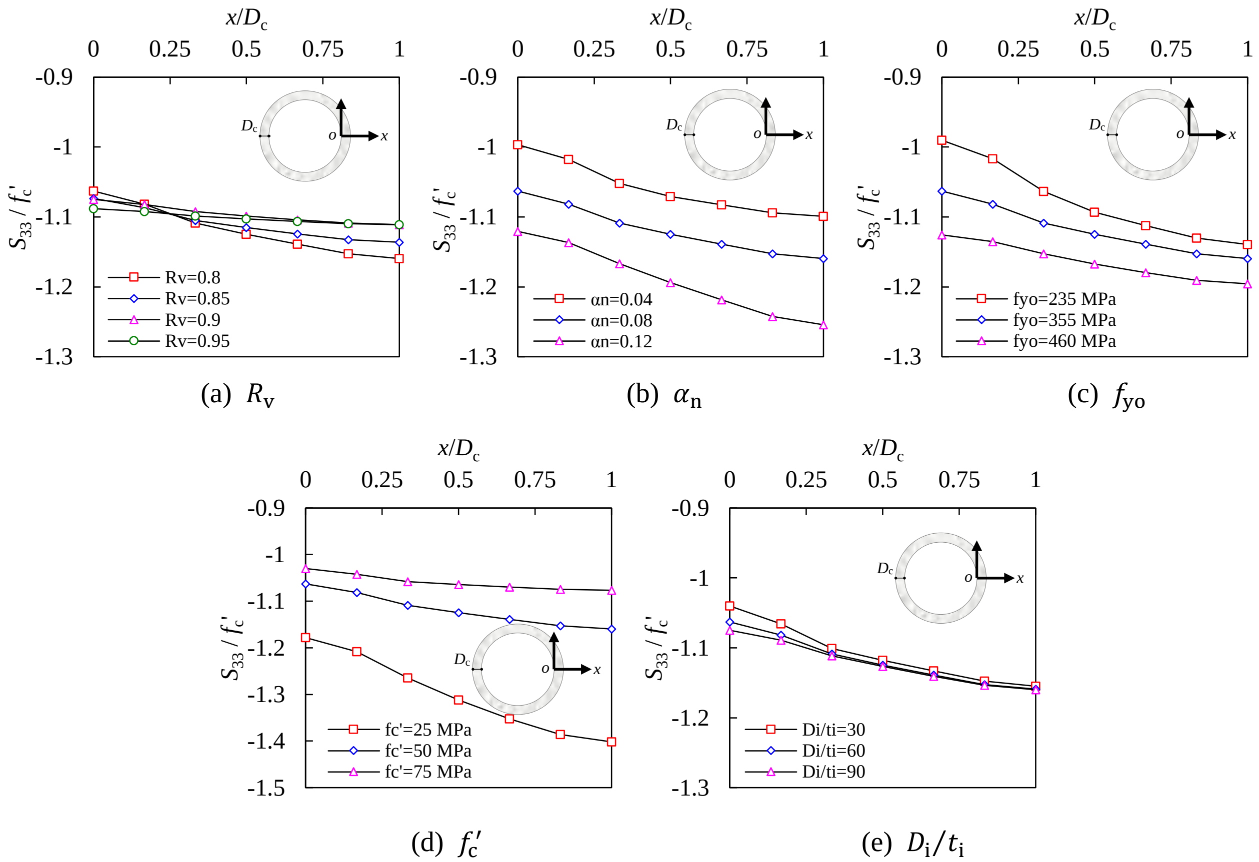

(a) R_v (b) α_n (c) f_{yo}

(d) f'_c (e) D_i/t_i

Fig. 18. Effect of parameters on S_{33}/f'_c of the concrete infill in the CFDST.

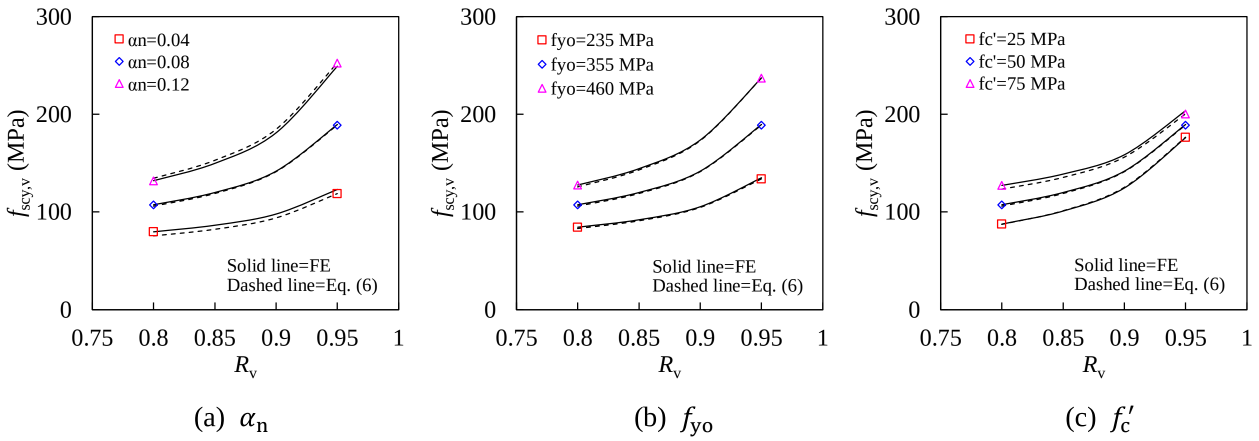

(a) α_n (b) f_{yo} (c) f'_c

Fig. 19. Effect of parameters on composite strength index ($f_{scy,v}$).

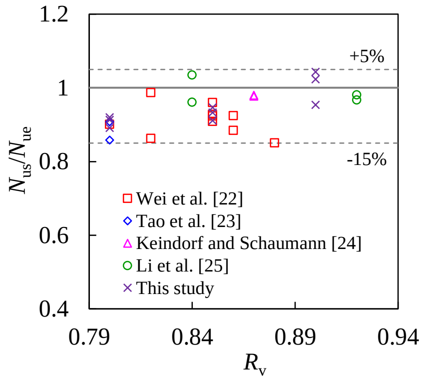

Fig. 20. Influence of R_{v} on $N_{\mathrm{us}}/N_{\mathrm{ue}}$.

Tables:

Table 1. Information of the specimens

No.	Label	$D_o \times t_o$ mm×mm	$D_i \times t_i$ mm×mm	D_o/t_o	D_i/t_i	R_v	f_{yo} (MPa)	f_{yi} (MPa)	f_{cu} (MPa)	K_e (×10^{6}kN)	N_{ue} (kN)	N_{ufe} (kN)	$\frac{N_{ufe}}{N_{ue}}$
1	Aa-0.8	538×3.76	418×5.63	143.1	74.2	0.8	253.8	296.3	66.6	5.707	8949.7	8321.3	0.930
2	Aa-0.85	538×3.76	449×5.63	143.1	79.8	0.85	253.8	296.3	66.6	5.272	7924.7	7310.8	0.923
3	Aa-0.9	538×3.76	477×5.63	143.1	84.7	0.9	253.8	296.3	66.6	4.145	6036.7	6329.8	1.049
4	Ab-0.8	538×3.76	418×5.63	143.1	74.2	0.8	253.8	296.3	49.4	5.505	7896.6	7070.8	0.895
5	Ab-0.85	538×3.76	449×5.63	143.1	79.8	0.85	253.8	296.3	49.4	4.337	6735.2	6391.6	0.949
6	Ab-0.9	538×3.76	477×5.63	143.1	84.7	0.9	253.8	296.3	49.4	3.565	5966.8	5725.8	0.960
7	Bb-0.8	538×5.63	420×5.63	95.6	74.2	0.8	296.3	296.3	49.4	6.306	8864.0	8199.6	0.925
8	Bb-0.85	538×5.63	448×5.63	95.6	79.8	0.85	296.3	296.3	49.4	5.478	8068.0	7487.0	0.928
9	Bb-0.9	538×5.63	473×5.63	95.6	84.7	0.9	296.3	296.3	49.4	4.367	6774.0	6795.3	1.003

Table 2. Properties of steel

Type	Thickness (mm)	f_y (MPa)	f_u (MPa)	E_s (×10^5 N/mm^2)	μ_s	δ_{ef} (%)
A	3.76	253.8	395.7	1.96	0.289	18.0
B	5.63	296.3	420.2	2.11	0.279	16.3

Table 3. Mix proportions and properties of the concrete

Type	Mix proportions (kg/m^3)						Properties			
	Cement	Fly ash	Coarse aggregate	Sand	Water	WRA*	$f_{cu,28}$ (MPa)	f_{cu} (MPa)	E_c (GPa)	Slump (mm)
a	420	130	832	800	189.5	11.62	54.2	66.6	35.9	270
b	325	208	911	790	103	7.20	30.6	49.4	33.6	245

*WRA=water-reducing admixture.